

PAPER


Wave propagation and absorption in a helicon plasma thruster and its plume

To cite this article: Pedro Jiménez *et al* 2022 *Plasma Sources Sci. Technol.* **31** 045009

View the [article online](#) for updates and enhancements.

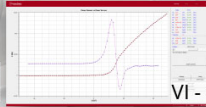
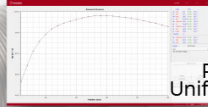
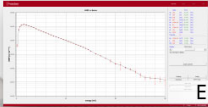
You may also like

- [Magnetic nozzle efficiency in a low power inductive plasma source](#)
T A Collard and B A Jorns
- [Diagnosis of helicon plasma by local OES](#)
Ruilin Cui, Ruoyu Han, Kaiyi Yang et al.
- [Modeling on plasma energy balance and transfer in a hollow cathode](#)
Shuai Cao, Junxue Ren, Haibin Tang et al.

**Intelligent Sensors for Plasma Monitoring and Diagnostics**

"The most advanced Langmuir Probe on the market"

Measures the characteristics of the bulk plasma region with an 80 MHz sampling rate. Pulse profiling and single shot plasmas can be measured with unrivalled time resolution.



EEPF Plasma Uniformity VI - Curve

Applications:

- RF-driven Plasmas
- Pulsed Plasma
- Atmospheric Plasma
- Magnetron Sputtering

Measures:

- EEDF
- Plasma Density
- Plasma & Floating Potential
- Electron Temperature

LEARN MORE

www.impedans.com

Wave propagation and absorption in a helicon plasma thruster and its plume

Pedro Jiménez^{*} , Mario Merino  and Eduardo Ahedo 

Equipo de Propulsión Espacial y Plasmas (EP2), Universidad Carlos III de Madrid, 28911 Leganés, Spain

E-mail: pejimene@ing.uc3m.es and <https://ep2.uc3m.es>

Received 15 November 2021, revised 7 March 2022

Accepted for publication 17 March 2022

Published 14 April 2022



CrossMark

Abstract

A two-dimensional, full-wave, frequency domain, cold plasma model is used to study electromagnetic power propagation and absorption in a helicon plasma thruster, including its far plume region and surrounding space. Results show that a fraction of power is absorbed in the plume region, and that the power deposition in the source is essentially unperturbed by the simulation domain size, the presence of metallic obstacles, or the plasma density in the environment. An electron–cyclotron resonance (ECR) surface always exists downstream that effectively prevents radiation to the space beyond along the plume. In the presence of an overdense environmental plasma, like the one expected in a vacuum chamber, fields are fully evanescent beyond this transition, and vacuum chamber boundary conditions affect but little the wavefields before this surface. In the absence of an environmental plasma, a double wave regime transition exists at the interface between the plasma and vacuum that hinders accurate numerical simulation in the plume region.

Keywords: waves in plasmas, electric propulsion, electrodeless thrusters, helicon plasma thruster

(Some figures may appear in colour only in the online journal)

1. Introduction

Helicon plasma thrusters (HPTs) are electric propulsion devices currently under research and development [1–9]. Their operation relies on the heating of a magnetically-confined plasma in a cylindrical vessel via oscillating electromagnetic fields generated with an inductor/antenna [10, 11], and the expansion and acceleration of that plasma in an external magnetic nozzle (MN), where magnetic thrust is generated before detachment occurs [12–14]. Being electrodeless, HPTs promise certain advantages compared to traditional electric propulsion technologies such as gridded ion thrusters or Hall thrusters, such as a potentially enhanced lifetime and the simplification of the overall system and electrical architecture [15]. The ease of control of the MN topology suggests a high throttability. Moreover, the absence of hollow cathodes with sensitive material inserts opens the possibility of using alternative propellants. However, reported thrust efficiencies are still below 20% [6, 16], and there are still open

questions in the understanding of the physical mechanisms that drive the performance of the HPT, in particular the problem of plasma heating by the electromagnetic waves.

The propagation and absorption of the electromagnetic fields is central to the operation of the device, and constitutes the object of study of the present work. These processes depend on the antenna geometry and currents, the shape of the source, the magnetic topology and strength, the plasma density map and, to a lesser extent, on the plasma temperature affecting the effective collisionality. In turn, the electromagnetic power deposition determines the plasma properties in the device. While the two aspects are intimately coupled, the timescale of the electromagnetic problem (10^{-7} s, or tens of MHz) is much faster than that of the plasma transport problem (ion transit times are in the order of 10^{-5} s). This enables the approximate study of these phenomena separately, an approach that has been successfully used to analyze the slow plasma dynamics in the source on the one hand [17–20], and the internal electromagnetic field problem on the other hand [21, 22].

^{*} Author to whom any correspondence should be addressed.

At the MHz-level frequencies used, typically 13.56 MHz, the ion response to the fast fields is negligible, and the electron response determines the propagation and absorption characteristics. For plasma densities n already greater than 10^{12} – 10^{13} m $^{-3}$ and applied magnetic field strengths B_a greater than 1–10 G, the excitation frequency ω is smaller than the electron plasma frequency ω_{pe} and the electron cyclotron frequency ω_{ce} , i.e. $\omega < \omega_{pe}, \omega_{ce}$. This means that the left-hand polarized (L) wave is evanescent and only the right-hand polarized (R) whistler wave propagates inside the HPT plasma, and only if its wavevector \mathbf{k} falls within a cone of half angle α_c about the magnetic field vector \mathbf{B}_a [23]. On the surface of this cone, $k \rightarrow \infty$ and therefore it is referred to as a resonance cone. Traditionally, this wave has been called helicon (H) wave [10, 24] (longer wavelengths) when \mathbf{k} is essentially parallel to \mathbf{B}_a , and Trivelpiece–Gould (TG) [25] waves (shorter wavelengths) when \mathbf{k} is essentially parallel to the resonance cone (and therefore has an important k_{\perp} component). For high B_a , there are some values of k_{\parallel} for which there are two solutions of k_{\perp} , one associated to the H wave and another to the TG wave. This is known as the double wave regime (DWR) [26]. In contrast, at lower B_a , only a single value of k_{\perp} exists for each propagating k_{\parallel} , this is known as the single wave regime (SWR). In general, both H and TG waves contribute to plasma heating, but a larger share of the power deposition is sometimes attributed to TG waves, especially near the surface of the plasma [27].

As the plasma expands into the MN, the magnetic field strength and plasma density gradually decrease. At some surface downstream in the plume, the electron–cyclotron resonance (ECR) eventually takes place where $\omega = \omega_{ce}$. With the typical operating frequency the resonant magnetic field strength is 4.84 G. Beyond the ECR surface, and as long as the plasma continues to be overdense ($\omega < \omega_{pe}$), the fields become evanescent. Eventually, the critical density transition ($\omega = \omega_{pe}$) is also reached, albeit typically this happens much farther out from the device.

Also, part of the electromagnetic excitation may leak out into the surrounding peripheral space. The situation here depends on the environmental conditions: in a perfect vacuum, both L and R waves propagate equally and unaffected by \mathbf{B}_a , with speed c and wavelength of tens of meters, obviously much larger than the device dimensions. At the interface between the dense HPT plasma and the vacuum, the L wave cutoff and the critical density transition are quickly traversed in succession.

However, in an environment with a tenuous plasma, propagation continues to be determined by n and \mathbf{B}_a . The ECR transition also exists in the peripheral space, and may affect the wavefields substantially. In particular, for plasma densities higher than the critical one, the propagation regime for R waves is qualitatively the same as inside the device—whistler waves propagating up to an angle with \mathbf{B}_a , and evanescence beyond the ECR surface. And, for densities roughly twice the critical value, the L wave does not propagate. These environmental conditions are relevant to experiments in laboratory vacuum chambers, which are intended to be representative of in-flight conditions, but where only a non-perfect vacuum may be achieved.

The simplest 1D radial models already show the presence of H and TG waves inside the cylindrical plasma source [21, 28, 29]; however, they miss the effect of axial nonuniformities in n and \mathbf{B}_a . Full-wave 2D asymmetric codes have been developed in the past to tackle this problem [30, 31], but under the assumption of an axially-aligned magnetic field $\mathbf{B}_a = B_{az}\mathbf{1}_z$. Recently, Tian *et al* [32] relaxed this limitation and included a small portion of the diverging MN plume in the model, enabling the analysis of the influence of the magnetic field topology on the wave propagation. Melazzi *et al* [21] used a different approach relaying on the method of moments to solve for the surface electric current density on the antenna and the volume polarization current within the plasma. Relatedly, Sánchez-Villar *et al* [33] presented a full-wave finite element method tool that has been successfully used for the simulation of a different type of electrodeless thruster, the electron cyclotron resonance thruster.

Existing studies of the electromagnetic fields in HPTs have been restricted to the plasma source and the very near plume. This leaves out several major questions on the propagation and absorption problem, such as whether this limited simulation domain is sufficient to understand power absorption by the plasma as a whole; or whether part of the radiofrequency (RF) radiation can escape downstream along the plume and be absorbed there. The role of the distant ECR surface has not been considered, to the best of our knowledge, in the operation of HPTs. Finally, it is relevant to ask what are the effects of the surrounding environment, i.e. whether a tenuous plasma or metallic obstacles can change the performance of the absorption by opening/closing propagation paths.

This work extends the 2D finite difference frequency domain (FDFD) model of [32] with an improved numerical implementation and interpolation routines for larger domains, and uses it to simulate the propagation and absorption of the RF fields in the source, surroundings, and far plume of an HPT, beyond the ECR surface, increasing the axisymmetric domain size from 15 cm to 67 cm axially and 2 cm to 20 cm radially, enabling the full simulation of the ECR transition. Furthermore, instead of a simple expansion for the plasma density and a constant collision frequency in the whole domain, a realistic map of plasma density is obtained from transport codes, one for the internal plasma dynamics [34], and another for the external expansion in the MN [12], and a collisionality map based on this density is used. Four different simulation cases are used to explore the questions above. Finally, we identify and comment on the modeling and numerical difficulties found when solving for the wavefields in the presence of critical density transition that takes place between the dense HPT plasma and a perfect vacuum.

The device of reference for the study is a medium size HPT (about 350–500 W) similar to the HPT05 prototype developed jointly by SENER Aeroespacial and UC3M [35].

The rest of this paper is structured as follows: section 2 describes the plasma-wave model, the numerical implementation, and the geometry and plasma profile inputs to the simulations. Section 3 provides a discussion of the electromagnetic fields and power deposition profiles obtained in four different simulation cases. Finally the difficulties of modeling

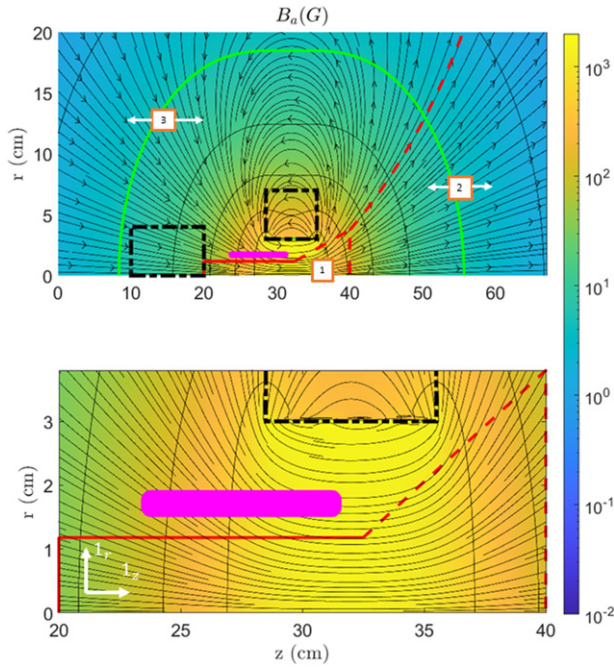


Figure 1. (Top) Simulation regions, applied magnetic field strength and field lines. The red line is the limit between the three different domains considered, the solid section corresponding to the plasma source. The green line depicts the electron cyclotron resonance location. The antenna is highlighted in magenta. The black dashed lines are additional conductor boundaries that represent thruster subsystems like the magnetic coils, structure, power processing unit, etc. (Bottom) Zoom of region 1.

and simulating the electromagnetic fields across critical density transitions, and the convergence of the numerical results, are surveyed in section 4. Section 5 gathers the conclusions of this work.

2. Electromagnetic model

The 2D, frequency-domain, electromagnetic model considers the physical domain represented in figure 1. The HPT source and its near plume are labelled as region 1, the magnetically guided far plume as region 2, and the periphery of the device as region 3. An axisymmetric plasma of known properties fills regions 1 and 2. The regions are determined based on the plasma transport code used to obtain the input profiles to the wave code as described in section 2.2. Additionally, an environmental plasma may exist in region 3, depending on the study case. With the exception of the axis of symmetry, the domain is terminated at metallic walls representing a vacuum chamber, which can be considered perfect conductors. Additionally, the magnetic coils and the HPT support equipment box (power processing unit, gas feed system, etc) inside the domain are treated as perfect-conductor metallic boxes.

The domain of figure 1 is excited by a known applied electric current \mathcal{J}_a at frequency $\omega/(2\pi) = 13.56$ MHz in the half-helical antenna located around the source. The applied magnetic field B_a is also shown in the figure. The B_a topology is slowly converging inside the source and diverging in the plume, with the magnetic throat placed approximately at

Table 1. Design and operational parameters.

Parameter	
Full simulation domain size	67 cm \times 20 cm
Chamber length l_c	12.5 cm
Chamber radius r_c	1.25 cm
Antenna type	Half-turn helical
Coil current	11×10^3 Ampere-turn
Antenna frequency $f = \omega/(2\pi)$	13.56 MHz
Antenna power	350 W
Antenna loop radius r_a	1.75 cm
Antenna length l_a	7.5 cm
Antenna central position z_a	27.5 cm
Antenna thickness d_t	0.5 cm
Propellant species	Xe
Propellant mass flow rate	1.0 mg s ⁻¹

the exit of the thruster tube. As the magnetic field strength decreases away from the source, an ECR surface appears on which $\omega = \omega_{ce}$. Following the nomenclature of [26], the plasma source and part of the plume is in the DWR, and only as B_a decreases, the plasma enters the SWR (near the ERC surface).

The HPT dimensions and characteristics are displayed in table 1. Four simulation cases are defined as follows:

Case R: this is the main simulation case and it is used as reference in the discussion. Region 3 is filled with a tenuous plasma of density $n = 10^{14}$ m⁻³, a reasonably low value for a typical laboratory vacuum chamber operation. This results in an overdense plasma in the peripheral space of the thruster. The internal metallic elements (coils, electronics ...) are treated as perfect electric conductors (PEC).

Case T: this case is identical to case R, except that the internal metallic boxes are removed from the simulation and therefore are transparent to the fields. The comparison of this case with case R illustrates the effect of obstacles on the propagation of the electromagnetic fields.

Case V: the difference with respect to case R is that the plasma density in region 3 is removed, $n = 0$, i.e. region 3 is a perfect vacuum. The comparison of this case with case R shows the influence of the environmental plasma, and the complexities associated with the critical density transition that takes place at the plasma-vacuum edge.

Case S: this smaller version of case R restricts the integration domain to region 1 and just the minimal part of region 3 to make the domain rectangular, with size [20–40] cm \times [0–4] cm.

In the following, we employ a cylindrical right-handed vector basis $\{\mathbf{1}_z, \mathbf{1}_r, \mathbf{1}_\theta\}$. The unitary vectors parallel and perpendicular to the locally applied magnetic field also allow forming an auxiliary vector basis, $\{\mathbf{1}_\parallel, \mathbf{1}_\perp, \mathbf{1}_\theta\}$.

2.1. Model formulation

A cold plasma model is used to describe the linearized plasma response to the electromagnetic fields. While the plasma itself is axisymmetric, we allow for non-axisymmetric fields, which

we decompose into azimuthal m modes. Any vector quantity $\mathcal{F}(z, r, \theta, t)$ is expressed as the real part of a superposition of such modes,

$$\mathcal{F}(z, r, \theta, t) = \Re \left[\sum_{m=-\infty}^{\infty} \mathbf{F}^m(z, r) \exp(-i\omega t + im\theta) \right], \quad (1)$$

where $\mathbf{F}^m(z, r)$ is the complex magnitude vector at $t = 0$, $\theta = 0$ for mode m . We do this, in particular, for the fast electric and magnetic fields \mathcal{E} and \mathcal{B} . Under these premises, the m th complex amplitude of the electric displacement field \mathcal{D} can be expressed as

$$\mathcal{D}^m(z, r) = \varepsilon_0 \bar{\bar{\kappa}}(z, r) \cdot \mathcal{E}^m(z, r), \quad (2)$$

where $\bar{\bar{\kappa}}(z, r)$ is the (axisymmetric) local cold plasma dielectric tensor [23], whose components in the vector basis $\{\mathbf{1}_{\parallel}, \mathbf{1}_{\perp}, \mathbf{1}_{\theta}\}$, after neglecting the contribution of ions, are:

$$\bar{\bar{\kappa}}(z, r) = \begin{pmatrix} P & 0 & 0 \\ 0 & (R+L)/2 & -i(R-L)/2 \\ 0 & i(R-L)/2 & (R+L)/2 \end{pmatrix}, \quad (3)$$

with

$$R = 1 - \frac{\omega_{pe}^2}{\omega(\omega + i\nu - \omega_{ce})},$$

$$L = 1 - \frac{\omega_{pe}^2}{\omega(\omega + i\nu + \omega_{ce})},$$

$$P = 1 - \frac{\omega_{pe}^2}{\omega(\omega + i\nu)};$$

where the electron cyclotron and plasma frequencies are defined as

$$\omega_{ce}(z, r) = \frac{eB_a}{m_e}, \quad \omega_{pe}(z, r) = \sqrt{\frac{ne^2}{m_e \varepsilon_0}}; \quad (4)$$

and the rest of symbols are conventional. The electron cyclotron and plasma frequencies, $\omega_{ce} \propto B_a$ and $\omega_{pe} \propto n^{1/2}$, are the main plasma parameters in the electromagnetic model, while the electron collisionality, ν , is secondary as long as $\nu/\omega \ll 1$. The ECR transition occurs when $\omega = \omega_{ce}$ and $R \rightarrow \infty$, while the critical density transition occurs when $\omega = \omega_{pe}$ and $P \rightarrow 0$. The L wave cutoff takes place when $L = 0$. The tensor $\bar{\bar{\kappa}}$ is rotated to the cylindrical vector basis used in the problem discretization.

To model the antenna current \mathcal{J}_a , we define the helicity number h as the number of complete turns of the antenna wire around the cylindrical source; for a half-turn helical antenna, $h = 0.5$. Inside the antenna, for $z \in [z_a - l_a/2, z_a + l_a/2]$ and $r \in [r_a - d_t/2, r_a + d_t/2]$, the axial current density is proportional to

$$\mathcal{J}_{za} \propto \delta\left(\theta - \frac{2\pi h}{l_a}(z - z_1)\right) - \delta\left(\theta - \pi - \frac{2\pi h}{l_a}(z - z_1)\right), \quad (5)$$

where δ is the Dirac delta distribution and $z_1 = z_a - l_a/2$. This equation represents the two wires of the antenna as they wind about the cylindrical source a number of turns determined by

the helix number (one full turn for $h = 1$). The antenna is 1D in the z, θ plane and has thickness d_t in the radial direction. For further reference in the modelling of helical antennas see [31, 36]. The radial current density \mathcal{J}_{ar} is zero, and the azimuthal current density is determined by continuity, $\nabla \cdot \mathcal{J}_a = 0$ [32]. As the electromagnetic problem is linear, the total current in the antenna is normalized to 1 A to compute the fields response.

Faraday's and Ampère's laws in (ω, m) space yield the following equations on the complex field amplitudes:

$$\frac{im}{r} E_z^m - \frac{\partial}{\partial z} E_{\theta}^m - i\omega B_r^m = 0, \quad (6)$$

$$\frac{\partial}{\partial z} E_r^m - \frac{\partial}{\partial r} E_z^m - i\omega B_{\theta}^m = 0, \quad (7)$$

$$\frac{1}{r} \frac{\partial}{\partial r} (r E_{\theta}^m) - \frac{im}{r} E_r^m - i\omega B_z^m = 0, \quad (8)$$

$$\frac{im}{r} B_z^m - \frac{\partial}{\partial z} B_{\theta}^m + i\omega \mu_0 D_r^m = \mu_0 J_{ar}^m, \quad (9)$$

$$\frac{\partial}{\partial z} B_r^m - \frac{\partial}{\partial r} B_z^m + i\omega \mu_0 D_{\theta}^m = \mu_0 J_{a\theta}^m, \quad (10)$$

$$\frac{1}{r} \frac{\partial}{\partial r} (r B_{\theta}^m) - \frac{im}{r} B_r^m + i\omega \mu_0 D_z^m = \mu_0 J_{az}^m, \quad (11)$$

As boundary conditions, the lateral and top walls in cases R, T, V and S are modelled as perfect electric conductors (PEC), and so are the support equipment boxes in cases R and V. PEC boundaries are characterized by a null tangential electric field $\mathbf{E} \times \mathbf{1}_n = 0$ and a null normal magnetic field $\mathbf{B} \cdot \mathbf{1}_n = 0$, where $\mathbf{1}_n$ is the unit normal vector to the domain boundaries. At the axis of symmetry, the following smoothness conditions apply for each mode m for any field \mathbf{F}^m [37],

$$F_r^m = F_{\theta}^m = 0 \quad \text{for } m = 0,$$

$$F_r^m = \mp i F_{\theta}^m, \quad F_z^m = 0 \quad \text{for } m = \pm 1,$$

$$F_r^m = F_{\theta}^m = F_z^m = 0 \quad \text{for } |m| > 1$$

(where the components of \mathbf{F} correspond to either \mathbf{E} or \mathbf{B}).

The plasma current density induced by the wave electric field is

$$\mathbf{J}_p^m = i\omega \varepsilon_0 (\bar{\mathbf{1}} - \bar{\bar{\kappa}}) \cdot \mathcal{E}^m, \quad (12)$$

where $\bar{\mathbf{1}}$ is the identity tensor and the time-averaged power density deposited into the plasma by mode m is $Q_a^m = \Re((\mathbf{J}_p^m)^* \cdot \mathcal{E}^m/2)$. The total resistive power seen at the antenna can be computed as the sum of the volume integral over the simulation domain for all the azimuthal modes,

$$P_a^m = \sum_m \int_{\Omega} Q_a^m d\Omega. \quad (13)$$

While we used a total power of 350 W to obtain the realistic plasma profiles from the transport simulations, observe that the wave problem is linear, and therefore fixing the antenna current at 1 A makes P_a numerically equal to the total resistance of the plasma, as seen by the antenna, and makes Q_a^m numerically equal to the local plasma resistivity, in SI units.

In the light of previous studies [20, 38] showing that the vast majority of the plasma resistance corresponds to the interaction of the electromagnetic fields with the currents in the azimuthal mode $m = 1$, this work focuses on this mode; the importance of higher modes is evaluated in section 3.

2.2. Magnetic field and plasma profiles

The cold plasma dielectric tensor $\bar{\kappa}$ at each point depends on the applied magnetic field \mathbf{B}_a , the plasma density n , and—to a lesser extent—the effective electron collisionality ν . The magnetic field \mathbf{B}_a , already shown in figure 1, is obtained analytically by modeling the magnetic coils of the device as a collection of current loops.

The plasma density n inside the source region 1, shown in figure 2, is obtained from the simulation of the plasma transport with the HYPHEN hybrid code [20]. The full details of HYPHEN can be found in [39]. This code solves the plasma properties in the source and near plume treating heavy species (ions and neutrals) kinetically and magnetized electrons as a fluid. Neutral gas injection, plasma sheaths, recombination at the walls and both elastic collisions and ionization are included in the model. Once HYPHEN reaches a stationary solution, the plasma density and ion flux at the right border of region 1 are used as the input to the open-source MN DIMAGNO code [12], which solves the plasma transport in region 2. DIMAGNO uses a fluid formulation for partially-magnetized ions and fully-magnetized electrons. The plasma collisions are neglected in the plume, and the supersonic plasma expansion is propagated using the method of characteristics. Notice that the HYPHEN domain (region 1) is polygonal while the DIMAGNO domain (region 2) follows the magnetic topology. A constant plasma density is imposed in region 3, which is outside of the domain of the transport codes, the value of this background density depends on the simulation case.

This approach combines the strengths of both transport codes, each specialized in one of the regions. As expected, the denser plasma is located in the source with values in the order of 10^{19} m^{-3} and decays rapidly in the plume to values near 10^{14} m^{-3} in the outer section. Finally, a low but nonzero constant value of $n = 10^{14} \text{ m}^{-3}$ is prescribed in region 3 in simulation cases R, T and S, representative of the operation inside a vacuum chamber with imperfect vacuum, while $n = 0$ is used in case V.

While HYPHEN evaluates several collisional elastic and inelastic processes in region 1, DIMAGNO assumes negligible collisionality in region 2 to compute the plasma transport solution. Since an effective electron collision frequency map ν is needed in the full domain for the wave code, HYPHEN's collisionality map is used in region 1, whereas in region 2 (and region 3 in simulation cases R, T, S), the map for e-i elastic collisions is used, $\nu = \nu_{ei} \sim nR_{ei}$, with

$$R_{ei} = \left(\frac{1 \text{ eV}}{T_e} \right)^{3/2} \times \ln \Lambda \times 2.9 \times 10^{-12} \text{ m}^3 \text{ s}^{-1}, \quad (14)$$

where $\ln \Lambda \approx 10$ is Coulomb's logarithm. A reference value, based on the conditions in the outer far plume of region 2, $T_e = 1 \text{ eV}$ is used in region 3. The reason to consider ν_{ei} as the

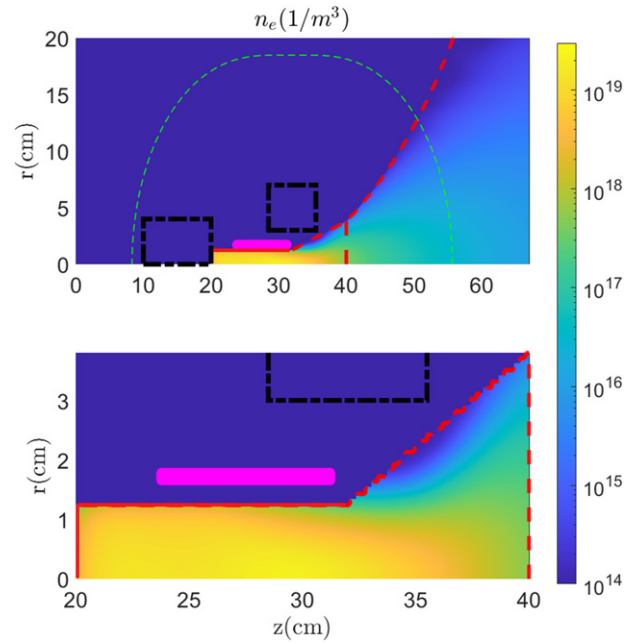


Figure 2. (Top) Plasma density for the reference case R in the simulation domain. (Bottom) Zoom at region 1.

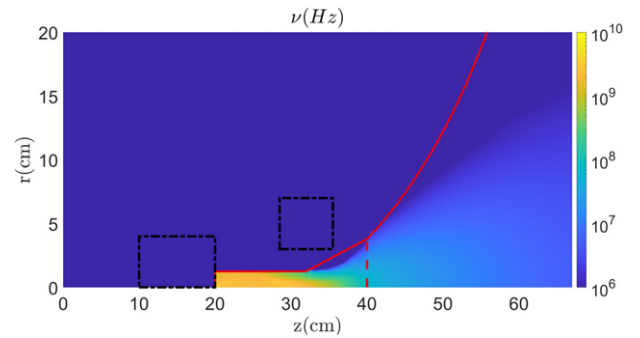


Figure 3. Effective collision frequency map. The numerical scaling factor has already been applied.

relevant map in these regions is that e-i collisions already dominate clearly compared to the second most important process, namely, e-n elastic collisions, at the interface between regions 1 and 2 (where the average values are $\nu_{ei} = 7.3 \times 10^5 \text{ Hz}$ and $\nu_{en} = 3.8 \times 10^4 \text{ Hz}$) and the difference is expected to grow along the plume. Finally, as explained at length in section 4 and after checking that this does not perturb the essential electromagnetic field solution nor the power deposition maps, collisionality is scaled up by a factor of 20 to improve numerical convergence. Figure 3 displays the used map of ν in the wave code.

2.3. Numerical integration

The numerical implementation of the model follows the general outline of [31, 32]. A brief summary of the main aspects of the integration approach are summarized next for self-completeness.

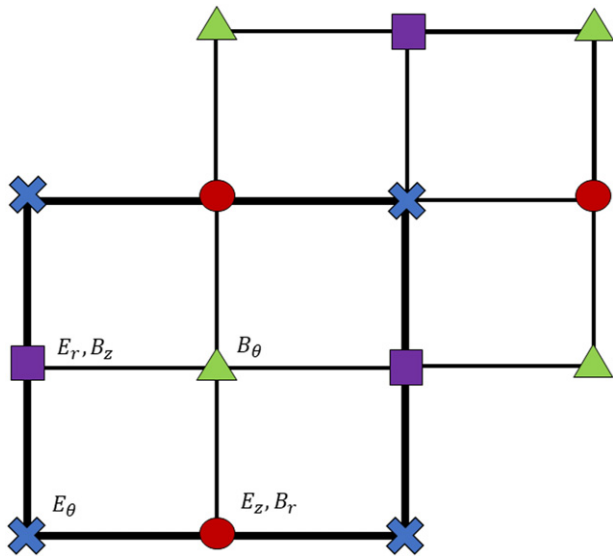


Figure 4. 2D staggered grid and electromagnetic fields. Each cell comprises a central node and four border nodes. E_θ is located in the blue X, E_z and B_r in the red circle, E_r and B_z in the purple square and finally B_θ in the green triangle.

The numerical solution of the electromagnetic fields in the frequency domain is obtained with a frequency domain finite difference method (FDFD), in particular, a modification of the well-known Yee's method [31, 40]. The use of staggered grids, on which only some components of the fields are stored, and depicted by different symbols in figure 4, allows for the direct discretization of equations (6)–(11) and for the easy implementation of boundary conditions. A major difference of a plasma with vacuum arises from the non-diagonal nature of tensor $\bar{\kappa}$, which couples each component of \mathbf{D} with all components of \mathbf{E} . This complicates the process of computing \mathbf{D} as only some components of \mathbf{E} are known on each node.

While in [38] this is accomplished by interpolating ($\kappa_{i,j}E_i$) from the surrounding nodes to the desired position, in this work we interpolate E_i only, and then multiply by the value of $\kappa_{i,j}$ at the desired position. The approach of [38] leads to good results when $\bar{\kappa}$ varies slowly, however, it was found to produce unacceptable high frequency noise at sharp transitions, and in particular at the critical density transition present in case V, when the mesh is not aligned with the transition. This is attributed to the imbalance between some of the components $\kappa_{i,j}$ used for the interpolation. Although the issue does not completely disappear with the new scheme, as further discussed in section 4, a numerical investigation has shown a reduction in the noise across this transition with the new interpolation scheme.

For a domain discretization with N_z cells in the axial direction and N_r cells in the radial direction, the set of $6 \times N_z \times N_r$ equations (including boundary conditions) is assembled into the linear system form $A\mathbf{x} = \mathbf{b}$, where A is the matrix of coefficients and \mathbf{b} is the forcing vector (containing the prescribed currents in the antenna). A direct solver is applied to obtain the electric and magnetic field components contained in the solution vector \mathbf{x} .

The results presented in the following section correspond the azimuthal mode number $m = 1$, with a grid a resolution

of 1000×1000 cells. The total number of degrees of freedom is 6 million and the computation time using a direct parallel linear solver was on the order of 100 min in a 32 core, 200 GB RAM computing node.

3. Results and discussion

In the reference simulation **case R** the plasma is over-dense everywhere, i.e. $\omega_{pe} > \omega$. Additionally, as explained in section 6, the metallic obstacles in the surroundings of the source are present in the simulation. The first row of figure 5 displays the magnitude and phase of E_θ^1 , i.e. the azimuthal electric field of mode $m = 1$. The RF field is clearly constrained by the ECR surface, as it must be evanescent beyond it. Overall, the field is strongest inside the cylindrical source (region 1), suggesting good coupling with the dense plasma. While the fields decay in the plume (region 2) and the periphery (region 3), it is evident that they are not zero: the electromagnetic fields propagate in these regions and are not confined to the source. Fields are small in the rear part of the cylindrical source. There is a partially-standing wave structure inside the plasma source, as evidenced by the localized drop in magnitude and the near 180 deg step. From the monotonic phase along the axis in region 2, a rightward-traveling wave exists up to the ECR surface, with an essentially-axial propagation direction. It is possible to estimate its wavelength to be around 20 cm by taking the distance for a full 360 deg phase cycle in the phase diagrams of figure 5. Notice that the wavelength is larger than the source tube due to the high magnetic field. This corresponds well with the analytical wavelength approximation for H waves, $\lambda \approx 2\pi d_e \sqrt{\omega_{ce}/\omega}$, where $d_e = c/\omega_{pe}$ is the local electron skin depth, for a plasma density $n \approx 5 \times 10^{17} \text{ m}^{-3}$ and a magnetic field intensity $B_a \approx 100 \text{ G}$ (resulting in $\omega_{pe} = 4.0 \times 10^{10} \text{ rad s}^{-1}$ and $\omega_{ce} = 1.8 \times 10^9 \text{ rad s}^{-1}$), which are characteristic values near the axis at $z \approx 40 \text{ cm}$. Interestingly, the analytical wavelength varies very little as both the density and magnetic field decrease along the plume.

Away from the axis, this axial wave develops a non-negligible k_\perp wavevector with increasing r , i.e. its propagation takes place at an angle with the magnetic field vector. The larger fields in the plume exist in a magnetic tube in this lateral region, indicating that \mathbf{B}_a defines to some extent the propagation paths of the electromagnetic fields. Propagation stops at the ECR surface, and the field magnitude drops quickly beyond it.

The electric field in region 3 is not negligible, especially close to the antenna, and its propagation is also affected by the direction of \mathbf{B}_a . Small wavelength structures of low magnitude can be observed in the space above the magnetic coils, where radiation is diffuse and standing wave patterns form. This radiation seems to be confined between the ECR surface in region 3 and the denser plasma of regions 1 and 2.

The power deposition profile, Q_a^1 is shown in the first panel of figure 6. The largest absorption is not correlated with the largest fields, and takes place inside the dense plasma in the cylindrical source ($\sim 95\%$). A non-negligible part of the power is absorbed downstream in the MN, before the ECR surface,

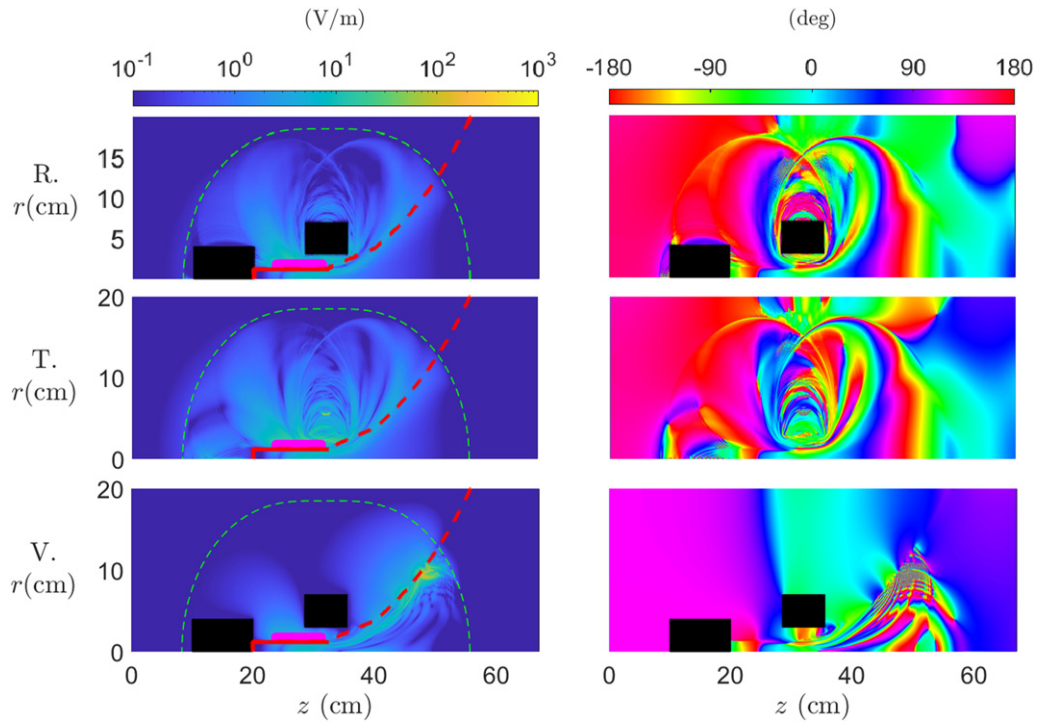


Figure 5. E_{θ}^1 field magnitude (left) and phase angle (right) for different simulation cases, for a total antenna current of 1 A. The electron cyclotron resonance line is depicted in green and the limit of the dense plasma in red.

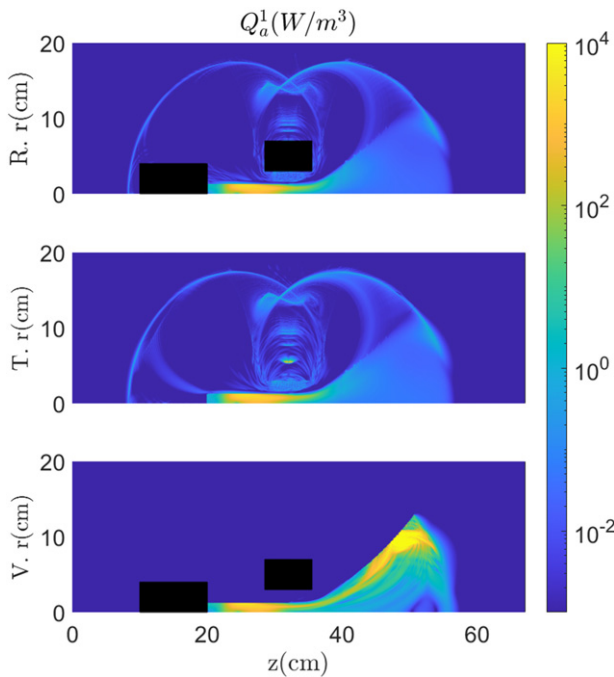


Figure 6. Power absorption maps Q_a^1 for the different simulation cases.

indicating the relevance of including this region 2 in the model to understand the power absorption.

A thin absorption layer exists at the ECR surface; however, this layer curves away from the ECR in the top part of the domain, in region 3, partially guided by the magnetic field vector. Less than 0.6% of the power emitted by the antenna

is absorbed in the space beyond the ECR surface, where the solution is evanescent. This result suggests that the ECR surface acts as an efficient shield to prevent radiation losses when operating in free space, i.e. to stop RF power from escaping the HPT plasma and its neighborhood, as long as the environment is overdense.

The removal of the metallic parts inside the domain in simulation **case T** does not result in any major changes in the wavefields nor the power deposition profile, as can be observed in the second row of figures 5 and 6. The only apparent difference is a slightly higher RF field traveling toward the rear part of the device, previously blocked by a metallic obstacle, and some additional absorption in the rear part of region 3. The small effect of these metallic boxes suggests that obstacles of this type essentially do not affect the solution.

Changing the environment into a perfect vacuum in **case V** has a far more dramatic effect on the RF fields (and on the accuracy of the numerical solution). This case is represented in the last row of figures 5 and 6. Firstly, the absence of plasma in region 3 also removes the possibility of a resonance at the ECR surface in this region, which now becomes transparent to the fields. Indeed, in the absence of plasma density, the value and direction of \mathbf{B}_a becomes irrelevant for the wave propagation problem. This means that the fields have access to the metallic boundary conditions that represent the vacuum chamber. Note that, in free space, any power traveling outward would give rise to radiation losses; however, in the present setup, representative of the operation in a laboratory vacuum chamber, this power is reflected back toward the domain by the boundary conditions, until all power is absorbed by the plasma in regions 1 and 2. The short-wavelength structures that existed in the

presence of a tenuous plasma in region 3 in case R disappear in case V, and radiation is partially delimited by the conductive boxes immersed in the domain. The ECR surface continues to be active in region 2, however. Secondly, fields in regions 1 and 2 become essentially a standing wave as evidenced by the node lines where $E_\theta^1 = 0$ in the magnitude plot of figure 5, suggesting that wall reflection indeed plays a role in this case. The propagation direction develops a major perpendicular component k_\perp to \mathbf{B}_a , and shorter wavelengths are observed, especially in the peripheral part of the MN plume. This suggests a more relevant role of the TG mode, which corresponds with shorter wavelengths and more perpendicular propagation than the H mode. As in previous cases, propagation within the plasma plume ends at the ECR. Thirdly, the importance of the fields in the plume is larger than in the previous cases, especially downstream, and so is the power absorption.

Notwithstanding these general observations, it is noted that simulation case V does not show the same numerical convergence characteristics in the plume region with mesh refinement as in the other cases. This issue, and its putative causes, are discussed in section 4.

Figure 7 displays a zoomed view of the power deposition profile the source region, and includes the small-domain simulation of **case S**. The four solutions show that the power absorption profile is essentially independent of the simulation case. This conclusion is valuable for two reasons. First, it supports the robustness of the modeling procedure, as changes in the details of the surrounding of the thruster have no major influence on the computation of power deposited inside the source, which accounts for the larger share of absorption. In fact, the power inside the source appears almost independent of the chamber conditions and the propagation in the plume. Second, these results show that, when only the computation of the power absorbed in the source is needed, it can be reliably obtained with a smaller simulation domain containing only this region (simulation case S).

Compared to the absorption map presented in [32] in which 2 to 3 stationary helicon wave cycles are visible inside the source, the deposition in figure 7 shows just one high absorption region covering much of the source. This is consistent with the plasma conditions used in this work (in particular, ≈ 1500 G at the axis), which differ from those of [32] (≈ 150 Gauss at the axis), resulting in an increase of the Helicon mode wavelength.

To conclude this section, the relevance of the azimuthal mode $m = 1$ is briefly discussed. Previous studies [10, 32] have already established the dominance of the $m = \pm 1$ azimuthal modes in the power coupling for different antenna types of helicon sources. Indeed, this antenna is designed to excite predominantly the $+1$ mode. Accordingly, the results presented above have considered this dominant mode only. To assess the validity of this approach, figure 8 compares the power absorption associated to $m = \pm 1, \pm 3$ in the whole domain of the simulation case R (the helical antenna only excites odd modes). As it can be inferred, after mode $m = +1$ the next mode in importance is $m = -1$. The power absorption of higher m modes drops quickly.

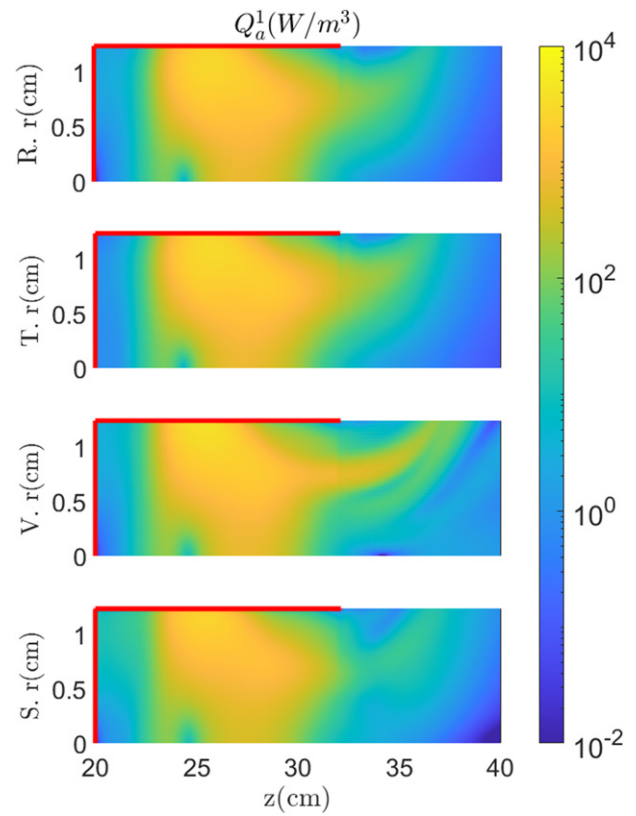


Figure 7. Power absorption maps Q_a^1 for the different simulation cases. Zoom at region 1.

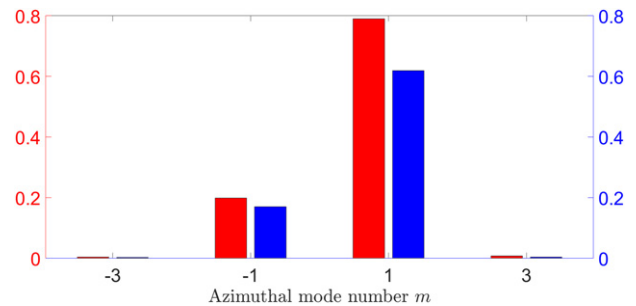


Figure 8. Fraction of total power (red) and fraction of power deposited inside the source (region 1, blue) for different azimuthal mode numbers, m .

4. Critical density transition and numerical convergence

The critical density transition takes place when $\omega = \omega_{pe}$, or equivalently, when $P = 0$ in equation (3). For an excitation frequency of 13.56 MHz, this happens when the plasma density drops below roughly $2.3 \times 10^{12} \text{ m}^{-3}$. In our simulations, this occurs only at the plasma–vacuum interface in case V.

The treatment of this transition presents a twofold difficulty. First, in the cold plasma dielectric tensor model and in the collisionless limit, the dispersion relation for an infinite uniform plasma with the critical density becomes singular, the $P = 0$ condition being a cutoff or a resonance depending on the direction of the propagation of the waves, given by the

wavevector \mathbf{k} [23]. This conditional/directional limit disappears strictly when collisions are present, but for small ν , the dielectric tensor $\bar{\bar{\kappa}}$ retains its wild, directional variation in the neighborhood of the transition. Indeed, near the critical density, electrostatic electron oscillation modes exist, whose description needs from thermal corrections. Therefore, the study of the electromagnetic fields in the vicinity of $\omega = \omega_{pe}$ cannot be properly approached from within the cold plasma model, and electron temperature effects need to be taken into account.

Second, but related to the first point above, the numerical discretization of the problem becomes ill-conditioned when the $P = 0$ transition is inside the domain, as in case V. Experience shows that this situation can give rise to spurious, highly oscillating fields near the transition, with wavelengths comparable to the numerical mesh. This problem is aggravated in the Cartesian numerical discretization employed in Yee's method wherever the grid directions differ substantially from the applied magnetic field direction at the transition ('staircase conditions'). Indeed, small wavelength structures are observed in case V in the plume-vacuum edge in region 2 (figure 5) that are linked to a highly-localized power deposition density (figure 6). These structures are insidious and could not be fully resolved with the available computational resources. They are seen to be smaller than the mesh size even in the finest simulation reported here. This phenomenon is not present near other regime transitions such as the ECR surface downstream ($R \rightarrow \infty$), where the fields are well-behaved in all simulations.

Figure 9 displays the error in the integrated power absorption of case R and case V for different grid sizes (mesh #), relative to the finest mesh simulations that was carried out (which are the ones reported in previous section),

$$\frac{|P_a^l(\text{mesh \#}) - P_a^l(\text{best mesh})|}{P_a^l(\text{best mesh})}.$$

In the light of the relevance of the power deposition in the source region 1, the convergence of this quantity is plotted too.

As it can be observed, the reference case R gradually converges, with errors below 2% inside the source for 1 million degrees of freedom, as shown in figure 9(b). Cases T and S behave essentially identically to case R, regarding convergence. This behavior gives confidence on the numerical convergence of the method, and the error trend agrees with the expected one for the used numerical scheme. On the other hand, the vacuum case V behaves differently. While the error in the source decreases roughly as in case R, indicating similar convergence characteristics there, the error in the whole domain does not diminish as the grid is refined. Far from it, the power deposited in the whole domain exhibits unsatisfactory values, driven by the spurious fields existing in the plume edge.

This convergence behavior was only observed in case V, and demonstrates the modeling and numerical difficulties commented on the above in the neighborhood of the critical plasma density transition. In all other simulation cases this interface is not associated to a parametric regime transition, and the only existing transition is the ECR surface downstream.

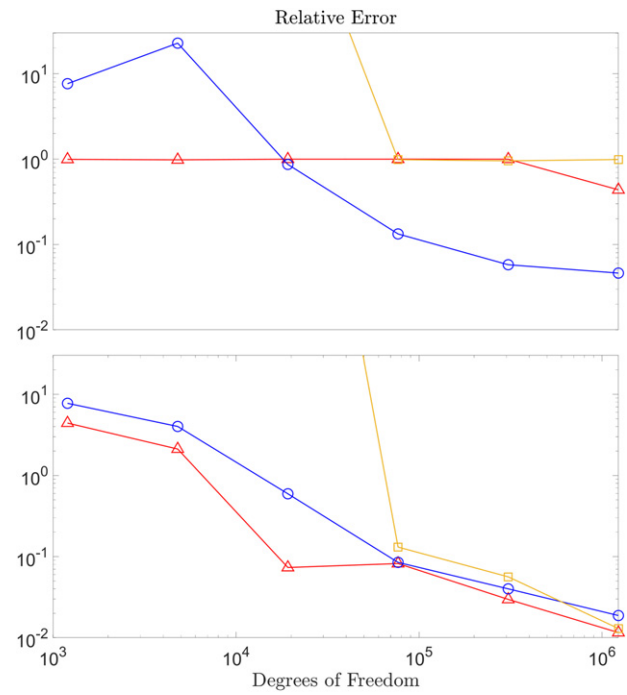


Figure 9. (Top) Error to the most accurate simulation of the power deposited in the full domain as a function of the degrees of freedom of the system (i.e. 6 times the number of Yee cells). Cases R (blue, \circ) and V (red, \triangle). The error with the previous interpolation scheme from [32] for case V is also shown for comparison (yellow, \square). (Bottom) Error for the power integrated only in region 1.

It is noted that smoothing out the plasma density profile near the edge does not solve the issue, as the $P = 0$ transition remains sharp and the $\bar{\bar{\kappa}}$ coefficients continue to vary rapidly across it. Several strategies are proposed to mitigate problems associated with these abrupt transitions, without requiring abandoning the cold plasma tensor formalism. Firstly, it is noted that increasing the imaginary component of P through added damping moves the zero away in the complex plane, improving the mathematical conditioning of the problem. A larger damping also helps suppress the small-wavelength noisy fields in a shorter distance. However, while this may be desirable to mitigate these oscillations, an excessively larger damping might hide some physical short wave-length structures. For this reason, after some numerical experimentation, a factor of 20 was used to scale collisionality in the problem, which improved convergence without altering essentially the solution.

Secondly, the transition noise was seen to be highly dependent on the interpolation strategy used in the Yee method to fix the value of \mathbf{D} at the nodes. It was observed that the interpolation scheme introduced in this work reduces the noise level and the error with respect to the former approach, proposed in [31] and used in [32]. The improvement is shown by the convergence lines of figure 9, specially by the faster convergence of the new scheme (red \circ) in the source with a limited number of degrees of freedom when compared to the former interpolation strategy (yellow \square). The enhanced convergence is directly linked to a reduction of noise along the $P = 0$ surface. It is

hypothesized that further exploration in this direction, as well as in the addition of auxiliary divergence equations near and at the transition, may help further improve the issue [41].

Thirdly, the fact that the mesh direction relative to \mathbf{B}_a affects the appearance of noise suggests that a mesh-aligned numerical discretization may also be instrumental in tackling it. Unfortunately, in the general case this would require irregular and non-structured meshes, for which finite difference methods are hard to implement. Much progress has been carried out in the field of finite elements for electromagnetic problems in the last decades, notably since the introduction of vector elements very successful in full-wave simulations [42]. This formulation is more suitable for non-structured and adaptable meshes. Indeed, finite elements have already been used with success to simulate the electromagnetic fields of other electric thrusters [33].

To conclude, it is noted that, in spite of this unsolved problem, the error associated to it seems to be local to a small region in the plume of case V. As shown in figure 9, this noisy region does not invalidate the convergence of the power deposited inside the source and near plume. While the solution in the plume region of case V is not acceptable and must be revisited in future work, the conclusions pertaining the power deposition in the source exhibit good convergence with mesh size and seem robust.

5. Conclusion

A finite-difference, frequency-domain, full-wave model has been used to investigate the propagation and absorption of electromagnetic fields in an HPT, including the far plume region and the surrounding space, with the goal of understanding the amount of power deposited in the plume and the influence of the environment in the electromagnetic problem. Plasma density and applied magnetic field coming from plasma transport simulations of a thruster similar to the HPT05 prototype were used as inputs in the study. While most of the power absorption occurs inside the cylindrical source, the fraction of power taken in by the plasma plume is not negligible. The fields propagate along the MN up to the ECR surface that always exists downstream. The wavelength and propagation direction corresponds to a helicon wave around the axis of the device. In the plume periphery, waves have a shorter wavelength and a more important perpendicular wave vector component, approaching the TG mode.

A tenuous plasma of density $n > 2.3 \times 10^{12} \text{ m}^{-3}$ in the neighborhood of the device and its plume suffices to make that region overdense ($\omega_{pe} > \omega$) for the usual excitation frequencies (13.56 MHz). This is the usual situation in laboratory vacuum chamber experiments, where pumping is not perfect. Even in a space environment, a faint low density plasma may envelope the thruster, keeping the effect of the ECR surface in the surrounding space active. In these conditions, the ECR surface has been shown to concentrate some of the power absorption and to play a fundamental role in confining the radiation away from the device, as the fields become evanescent beyond it. This, in particular, has great relevance for the ‘free space’ representativeness of finite-size vacuum chamber

experiments which are normally made of conductive metal, and therefore constitute a closed, reflective cavity for the fields. If the ECR surface is located within the chamber, the effect of these reflective walls on the fields becomes negligible, as they are in contact only with the region of space where fields are evanescent.

In strict vacuum, the ECR surface plays no role in the surrounding space, as in this case there are no electrons to resonate with the fields, and a path for radiation losses opens up in the radial direction away from the thruster (but not along the plume, where the plasma continues to be overdense and fields continue to be evanescent beyond the ECR transition). Indeed, the propagation and absorption maps change and exhibit standing-wave structures as a consequence of the reflective bounding box used in the simulation.

The influence of reflective boxes inside the domain (representing support equipment of the thruster) was seen to be small. Moreover, the power absorption in the source region was seen to be stable and essentially the same across simulations, suggesting that all aspects that affect the plume and the environmental region are superfluous for the source power absorption. This adds confidence to the small-domain, source-only simulations carried out in previous works, albeit they miss the information of the power absorption in the plume.

Finally, numerical convergence studies showed good convergence characteristics for all cases except the vacuum environment one, where the strong and ill-conditioned critical density transition surface at the interface between the plasma plume and vacuum, plus the numerical staircase mesh conditions there, are identified as the sources of small-scale numerical noise. The implementation used in this work is based on a new interpolation scheme which partially mitigates this problem and restricts noise to a small region without affecting results much elsewhere. Notwithstanding this, future work must address the theoretical modeling and the numerical treatment of these transitions. Some additional avenues of research have been suggested in section 4, namely the use of enhanced damping in this region, and aligning the mesh geometry to the transition, perhaps by switching to other schemes such as finite elements to simplify the implementation of unstructured meshes.

The validation against experimental data of the present wave model requires direct measurement of the electromagnetic fields and their phase, notably inside the plasma source, without perturbing the operation of the thruster. Currently, no such data is known to exist to the authors. However, coupled plasma transport and wave simulations (employing the same FDTD solver as this work) compare reasonably well to experimental studies with a similar HTP setup in terms of indirect measurements such as thrust and several efficiencies. In particular for the HPT05 prototype, numerical [20] and experimental [6] results show about 30% relative discrepancy in key performance figures like thrust efficiency in similar operation regimes (although the comparison is not perfect, as the configuration of [6] has a slightly higher antenna power). Further work in this direction and new, more precise experimental measurements, are still necessary to close the validation gap.

Acknowledgments

The authors want to thank the developers of the HYPHEN code, specially J Zhou and A Domínguez-Vázquez. The work of Pedro Jiménez has been supported by the HIPATIA project, funded by the European Union's Horizon 2020 Research and Innovation Program, under Grant Agreement Number 870542. The work of Mario Merino and Eduardo Ahedo has been supported by the PROMETEO project, funded by the Comunidad de Madrid, under Grant reference Y2018/NMT-4750 PROMETEO-CM.

Data availability statement

The data that support the findings of this study are available upon reasonable request from the authors.

ORCID iDs

Pedro Jiménez  <https://orcid.org/0000-0003-3244-5410>

Mario Merino  <https://orcid.org/0000-0001-7649-3663>

Eduardo Ahedo  <https://orcid.org/0000-0003-2148-4553>

References

- [1] Ziemba T, Carscadden J, Slough J, Prager J and Winglee R 2005 High power helicon thruster *41st AIAA/ASME/SAE/ASEE Joint Propulsion Conf. & Exhibit, AIAA 2005-4119*
- [2] West M D, Charles C and Boswell R W 2008 *J. Propul. Power* **24** 134–41
- [3] Pavarin D et al 2009 Design of 50 W helicon plasma thruster *31st Int. Electric Propulsion Conf., IEPC 2009-205*
- [4] Ahedo E 2013 Plasma Dynamics in a Helicon Thruster, Progress in Propulsion Physics (*EUCASS Proc. Series - Advances in AeroSpace Sciences* vol 4) ed L T DeLuca, C Bonnal, O J Haidn and S M Frolov (Bruxelles: European Conference for Aerospace Sciences) pp 337–54
- [5] Ahedo E and Navarro-Cavallé J 2013 *Phys. Plasmas* **20** 043512
- [6] Navarro-Cavallé J, Wijnen M, Fajardo P, Merino M and Ahedo E 2017 Experimental performances of a 1 kW HPT by means of plasma diagnostics *35th Int. Electric Propulsion Conf., No. IEPC-2017-447* (Atlanta, GA: Electric Rocket Propulsion Society)
- [7] Batishchev O V 2009 *IEEE Trans. Plasma Sci.* **37** 1563–71
- [8] Navarro-Cavallé J, Wijnen M, Fajardo P, Ahedo E, Gómez V, Giménez A and Ruiz M 2019 Development and characterization of the helicon plasma thruster prototype HPT-03 *36th Int. Electric Propulsion Conf., No. IEPC-2019-596* (Vienna, Austria: Electric Rocket Propulsion Society)
- [9] Takahashi K 2019 *Rev. Mod. Plasma Phys.* **3** 3
- [10] Chen F F 1991 *Plasma Phys. Control. Fusion* **33** 339
- [11] Chen F F 1996 *Phys. Plasmas* **3** 1783–93
- [12] Ahedo E and Merino M 2010 *Phys. Plasmas* **17** 073501
- [13] Merino M and Ahedo E 2016 *Magnetic Nozzles for Space Plasma Thrusters, Encyclopedia of Plasma Technology* ed J L Shohet vol 2 (London: Taylor and Francis) pp 1329–51
- [14] Martínez-Sánchez M, Navarro-Cavallé J and Ahedo E 2015 *Phys. Plasmas* **22** 053501
- [15] Ahedo E 2011 *Plasma Phys. Control. Fusion* **53** 124037
- [16] Takahashi K 2021 *Sci. Rep.* **11** 1–12
- [17] Chen G and Raja L L 2004 *J. Appl. Phys.* **96** 6073–81
- [18] Bose D, Govindan T R and Meyyappan M 2003 *IEEE Trans. Plasma Sci.* **31** 464–70
- [19] Magarotto M, Melazzi D and Pavarin D 2020 *Comput. Phys. Commun.* **247** 106953
- [20] Zhou J, Pérez-Grande D, Fajardo P and Ahedo E 2019 *Plasma Sources Sci. Technol.* **28** 115004
- [21] Melazzi D and Lancellotti V 2014 *Comput. Phys. Commun.* **185** 1914–25
- [22] Jiménez P, Merino M and Ahedo E 2021 Preliminary investigation of the electromagnetic fields in the far plume of a helicon plasma thruster *Space Propulsion Conf. 2021, No. 00331* (Association Aéronautique et Astronautique de France)
- [23] Stix T H 1992 *Waves in Plasmas* (Berlin: Springer)
- [24] Breizman B N and Arefiev A V 2000 *Phys. Rev. Lett.* **84** 3863–6
- [25] Blackwell D D, Madziwa T G, Arnush D and Chen F F 2002 *Phys. Rev. Lett.* **88** 145002
- [26] Chen F F and Arnush D 1997 *Phys. Plasmas* **4** 3411
- [27] Chen X and Sanmartín J R 2015 *Phys. Plasmas* **22** 053504
- [28] Chen F F 2008 *IEEE Trans. Plasma Sci.* **36** 2095–110
- [29] Tian B, Ahedo E and Navarro J 2014 Investigation of plasma-wave interaction in helicon antenna thrusters *50th AIAA/ASME/SAE/ASEE Joint Propulsion Conf.*
- [30] Mouzouris Y and Schärer J E 1998 *Phys. Plasmas* **5** 4253–61
- [31] Chen G, Arefiev A V, Bengtson R D, Breizman B N, Lee C A and Raja L L 2006 *Phys. Plasmas* **13** 123507
- [32] Tian B, Merino M and Ahedo E 2018 *Plasma Sources Sci. Technol.* **27** 114003
- [33] Sánchez-Villar Á, Zhou J, Ahedo E and Merino M 2021 *Plasma Sources Sci. Technol.* **30** 045005
- [34] Domínguez-Vázquez A 2019 Axisymmetric simulation codes for Hall effect thrusters and plasma plumes *PhD Thesis* Universidad Carlos III de Madrid, Leganés
- [35] Navarro-Cavallé J, Wijnen M, Fajardo P and Ahedo E 2018 *Vacuum* **149** 69–73
- [36] Kamenski I V and Borg G G 1996 *Phys. Plasmas* **3** 4396
- [37] Jin J-M and Riley D J 2009 *Finite Element Analysis of Antennas and Arrays* (New York: Wiley)
- [38] Tian B 2017 Modeling of physical processes in radio-frequency plasma thrusters *PhD Thesis*
- [39] Zhou J, Jiménez P, Merino M, Fajardo P and Ahedo E 2019 Numerical simulations of the plasma discharge in a helicon plasma thruster *36th Int. Electric Propulsion Conf., No. IEPC-2019-330* (Vienna: Electric Rocket Propulsion Society)
- [40] Kane Yee K 1966 *IEEE Trans. Antennas Propag.* **14** 302–7
- [41] Munz C-D, Omnes P, Schneider R, Sonnendrücker E and Voss U 2000 *J. Comput. Phys.* **161** 484–511
- [42] Nédélec J C 1980 Mixed finite elements in \mathbb{R}^3 *Numer. Math.* **35** 315–41